Eur. Phys. J. C (2026) 86:24
https://doi.org/10.1140/epjc/s10052-025-15254-y

THE EUROPEAN PHYSICAL JOURNAL C

Regular Article - Theoretical Physics

Search for imprints of isovector–scalar mesons and kaon condensation in binary neutron star inspiral gravitational waves

Bin Hong[1,a], **ZhongZhou Ren**[1,2,b]

[1] School of Physics Science and Engineering, Tongji University, Shanghai 200092, China
[2] Key Laboratory of Advanced Micro-Structure Materials, Ministry of Education, Shanghai 200092, China

Received: 5 November 2025 / Accepted: 20 December 2025

Abstract Gravitational wave signals emitted during the binary neutron star inspiral phase offer a promising avenue for probing stellar internal composition. Isovector–scalar mesons and kaon condensation are thought to play pivotal roles in characterizing asymmetric nuclear matter and constraining the dense nuclear equation of state. This study explores whether their potential effects in neutron stars can be identified from inspiral gravitational wave frequencies, retarded times and orbital phases. Our analysis reveals the isovector–scalar meson accelerates the inspiral process, leading to shorter retarded times and lower maximum gravitational wave frequencies compared to standard binary neutron star systems, while binary systems influenced by kaon condensation exhibit even shorter inspiral retarded times and lower gravitational wave frequencies than those influenced solely by isovector–scalar mesons. Quantitatively, the incorporation of kaon condensation leads to a reduction of approximately 200 Hz in the maximum inspiral gravitational wave frequency, and the variations in retarded times across different kaon potentials reach approximately five milliseconds, whereas the corresponding variations induced by isovector–scalar mesons are around one millisecond. Combined with observable mass–radius relationships and tidal deformabilities, our findings strongly suggest that inspiral gravitational wave signals could serve as a strategic probe for identifying potential isovector–scalar and kaon mesons.

1 Introduction

Exploring the properties of matter at extreme high densities has been a long-standing pursuit in the scientific community. Neutron stars (NSs), the compact remnants of massive stellar explosions and predominantly composed of neutrons at ultra densities, act as natural laboratories for probing the fundamental matter behaviors [1–3]. Recent astronomical observations have significantly advanced our understanding of NSs. Notable milestones include the first detection of nearly two times solar mass ($M_\odot$) NSs of PSR J1614-2230 [4,5] and PSR J0348+0432 [6], as well as precise mass–radius measurement from NICER (Neutron Star Interior Composition Explorer) for PSR J0030+0451 [7,8], PSR J0740+6620 [9,10], and PSR J0437-4715 [11]. Additionally, the identification of a massive compact companion with a mass of $2.5\sim2.67M_\odot$ in GW190814 [12], alongside the observations of the fastest/heaviest black widow pulsar PSR J0952-0607 [13] with a mass of $2.35 \pm 0.17M_\odot$, continue to push the NS mass boundaries. In contrast to massive NS limit, an extremely low-mass compact object of $M = 0.77^{+0.20}_{-0.17}M_\odot$ in the supernova remnant HESS J1731-347 [14] and a plausible NS companion with $M = 1.174M_\odot$ in compact binary system J0453+1559 [15], further reshape our understanding of NSs. Fortunately, the landmark detection of binary NS merger GW170817 by the LIGO/Virgo Collaborations [16], have opened unprecedented avenues for exploring the internal composition and equation of state (EoS) of NSs from the view of gravitational waves. Despite these recent advancements, the detection of gravitational wave events remains markedly scarce, and seriously, significant uncertainties continue to surround the microscopic interactions that govern dense nuclear matter, particularly the role of exotic states and components in NS interiors still requires continued collaborative efforts from the scientific community [2,3].

A central unresolved issue is the precise nature of the EoS for neutron-rich matter at high densities [17,18], as it governs the macroscopic properties of NSs, including their mass–radius relationship and maximum mass limit. Within nuclear many body field, as a phenomenological method

[a] e-mail: hongbin@tongji.edu.cn (corresponding author)
[b] e-mail: zren@tongji.edu.cn

Published online: 14 January 2026

to model the EoSs, the relativistic mean-field (RMF) theory [19–21] accounting for neutrons and protons interaction via meson exchanges is commonly employed, since it demonstrates unique advantages in dealing with high-density nuclear matter environments, particularly suitable for studying astrophysical objects like NSs [22–28]. Recently, the inclusion of additional meson degrees of freedom, particularly isovector–scalar δ mesons [29,30], have garnered attention for their potential impact on the properties of nuclear matter properties. Incorporating these mesons into RMF models is expected to modify the symmetry energy and its slope, both of which are key factors for accurately modeling finite nuclei and infinite nuclear matter properties from available experimental data [31,32], also essential for determining the structure and stability of NSs [33–36]. Furthermore, given that the densities within NSs are several times that of saturation nuclear matter, the emergence of new degrees of freedom, such as hyperons [37,38], quarks [39–44], dark matters [45], and kaon condensation [46,47] become plausible. Kaon meson (K^-) condensation, as a theoretical hypothetical accumulation of a Bose–Einstein condensate within the cores of massive NSs [48–50], is predicted to occur under extremely dense environments and holds profound implications for observable phenomena, including the stellar EoSs [46,47], superfluidity dynamics [49], and thermal evolution [51,52], highlighting its critical role in shaping NS properties. Inclusion of a isovector–scalar meson δ into the NSs with kaon meson condensation and a study of their role in binary NS inspiral gravitational wave signals is still underexplored.

The inspiral phase of binary NS (BNS) mergers offer an unparalleled window for probing NS internal structure through gravitational wave characteristic signals [53]. The inspiral phase carry distinctive signatures of the tidal deformability, which in turn shed light on the intricate structural properties of the NSs [54–58]. Meanwhile, the gravitational wave frequency, retarded time, and gravitational waveform during the BNS inspiral phase also contain useful information about the NS interior. Recent studies have underscored the role of inspiral phase gravitational waves in revealing the structure of NS composition [59–61]. In this study, we aim to investigate the effects of isovector–scalar mesons within the RMF framework on the NS properties with kaon condensation during the BNS inspiral process, and try to seek the potential signals of isovector–scalar δ mesons and kaon condensation from BNS inspiral gravitational waves.

The structure of this paper is as follows: Sect. 2 will detail how isovector–scalar mesons are introduced to describe NS matter within the RMF theory, and how kaon condensation is treated in the same framework. Section 3 examines the impact of isovector–scalar mesons on key physical properties of NSs with kaon condensation, including tidal deformabilities, inspiral gravitational wave frequencies, inspiral retarded times, and waveform characteristics. We will also explore how these properties can be used to potentially identify signals from isovector–scalar mesons and kaon condensation. Finally, Sect. 4 provides a brief summary.

2 Microscopic models

2.1 Isovector–scalar mesons in RMF theory for baryon matter models

Within the framework of RMF theory [19–21], nucleon interactions are mediated by the exchange of different mesons. The typical representation includes the scalar–isoscalar meson σ, which accounts for the medium-range attractive nuclear force, the vector–isoscalar meson ω, responsible for short-range repulsion and the vector–isovector meson ρ, which captures the effects of nucleon isospin. In this work, we adopt a streamlined version known as the "$\sigma\omega\rho$" meson exchange model and incorporate the isovector–scalar meson δ under this framework [29,30,36,62]. This approach effectively highlights the essential aspects of RMF theory and has been extensively employed to describe isospin asymmetry matter at high densities, as well as the NS properties [26,27]. The corresponding nonlinear Lagrangian density in NS system incorporating of isovector–scalar meson δ can be expressed as follows [29]:

$$
\begin{aligned}
L = & \sum_{N=n,p} \bar{\psi}_N \Big(\mathrm{i}\partial_\mu \gamma^\mu - m_N + g_\sigma \sigma - g_\omega \omega_\mu \gamma^\mu + g_\delta \boldsymbol{\delta} \cdot \boldsymbol{\tau} \\
& - \frac{1}{2} g_\rho \boldsymbol{\rho}_\mu \gamma^\mu \cdot \boldsymbol{\tau} \Big) \psi_N + \frac{1}{2} \partial_\mu \sigma \partial^\mu \sigma - \frac{1}{2} m_\sigma^2 \sigma^2 - \frac{1}{4} g_3 \sigma^4 \\
& - \frac{1}{4} \boldsymbol{\rho}_{\mu\nu} \boldsymbol{\rho}^{\mu\nu} + \frac{1}{2} m_\rho^2 \boldsymbol{\rho}_\mu \boldsymbol{\rho}^\mu - \frac{1}{4} \omega_{\mu\nu} \omega^{\mu\nu} + \frac{1}{2} m_\omega^2 \omega_\mu \omega^\mu \\
& - \frac{1}{3} g_2 \sigma^3 + \Lambda_\omega \left(g_\rho^2 \rho^\mu \rho_\mu \right) \left(g_\omega^2 \omega^\mu \omega_\mu \right) \\
& + \frac{1}{2} \left(\partial_\mu \delta \partial^\mu \delta - m_\delta^2 \delta^2 \right) + \frac{\zeta}{4!} g_\omega^4 \left(\omega_\mu \omega^\mu \right)^2 \\
& + \sum_{l=e,\mu} \bar{\psi}_l \left(i \partial_\mu \gamma^\mu - m_l \right) \psi_l, \qquad (1)
\end{aligned}
$$

with N and l being nucleons (n, p) and leptons (e, μ) in the NS beta-equilibrium system, and m_i (where $i = N$, l, σ, ω, ρ, δ) being the mass of nucleons, leptons and mesons. The nucleon Dirac effective mass is denoted by $m_N^* = m_N - g_\sigma \sigma - g_\delta \boldsymbol{\delta} \cdot \boldsymbol{\tau}$ and the coupling constants of g_σ, g_ω, g_ρ, g_δ, g_2, g_3, Λ_ω, ζ are typically calibrated to empirical saturation characteristics like saturation density n_0, per nucleon binding energy B/A, effective mass m^*, incompressibility coefficient K, symmetry energy J_{sym} and its slope L. Renowned parameter sets such as FSUGold [63], NL3 [64], BigApple [65], IOPB-I [31], FSUGarnet [66], DOPS series [67] and OMEG series [68] are frequently

Table 1 The nucleon coupling parameters of BigApple [65] and RMFSET [69] as well as their corresponding isovector–scalar revised version for using symmetry energy slopes $L = 80$ MeV and $L = 90$ MeV

	BigApple			RMFSET		
	Original	δ ($L = 80$)	δ ($L = 90$)	Original	δ ($L = 80$)	δ ($L = 90$)
g_σ	9.669	8.963	8.603	9.846	8.879	8.328
g_ω	12.316	9.899	9.704	10.746	10.558	10.377
g_ρ	14.161	15.095	15.926	9.9829	11.084	11.751
g_2	11.91	12.75	13.41	20.43	22.73	23.56
g_3	− 31.67	− 29.34	− 25.54	− 43.17	− 37.71	− 33.80
ζ	0.0007	0.0007	0.0007	0.0	0.0	0.0
Λ_ω	0.0474	0.0386	0.0292	0.0314	0.0174	0.0085
g_δ	0.0	5.057	6.163	0.0	5.790	6.961

employed in RMF theory to model NSs. In this study, we employed two calibrated relativistic parameter sets for comparable analysis. One is the BigApple set [65], which is proposed based on the ground state properties of finite nuclei and observations of massive NSs. Another set, referred to here as RMFSET [69], follows the methodology outlined in [69], and this set establishes a clear mathematical relationship between nucleon couplings and nuclear saturation properties, with its foundational derivation accessible through [69,70]. Our analysis in RMFSET adopts nuclear saturation values of $n_0 = 0.15$ fm^{-3} [71], $K = 240$ MeV [72], $E/A = -16$ MeV [69], $m_N^*/m_N = 0.70$ [69], $J_{\rm sym} = 32$ MeV [73], $L = 60$ MeV [2], and they give corresponding coupling constants being $g_\sigma = 9.846$, $g_\omega = 10.746$, $g_\rho = 9.9829$, $g_2 = 20.43$ fm^{-1}, $g_3 = -43.17$, $\Lambda_\omega = 0.0314$. To characterize the influence of the isovector–scalar meson δ on gravitational wave properties, we parameterize its effects through the symmetry energy slope L, given that the coupling constant of the δ meson to nucleons is directly determined by this parameter. In this study, we employ representative symmetry energy slope values of $L = 80$ MeV and $L = 90$ MeV as benchmarks for our analysis. The nucleon coupling parameters for the BigApple [65] and RMFSET [69] parameter sets, along with those for their corresponding isovector–scalar revised versions, are shown in Table 1.

2.2 Kaon condensation in RMF theory

At baryon densities of several times the nuclear saturation value, the electron Fermi energy rises sufficiently to render electron be captured by protons, producing negatively charged kaons K^- [48,74–76]. Within the RMF framework, the Lagrangian incorporates the kaon degrees of freedom will be written as follows [47,49,77,78]:

$$\mathscr{L}_{K^-} = \mathscr{D}_\mu^* K^{-*} \mathscr{D}^\mu K^- - m_{K^-}^{*2} K^{-*} K^-, \tag{2}$$

where the covariant derivative $\mathscr{D}_\mu = \partial_\mu + i g_{\omega K^-} \omega_\mu + i g_{\rho K^-} \boldsymbol{\tau}_{K^-} \boldsymbol{\rho}_\mu$, and the in-medium kaon mass is $m_{K^-}^* = m_{K^-} - g_{\sigma K^-}\sigma$. Guided by SU(3) flavor symmetry, the vector coupling constants are typically set as $g_{\omega K^-} = \frac{1}{3} g_\omega$, $g_{\rho K^-} = g_\rho$ [49,77,79], while the scalar coupling $g_{\sigma K^-}$ is determined phenomenologically from the kaon optical potential at n_0 [47,49,77]:

$$U_{K^-}(n_0) = -g_{\sigma K^-}\sigma_0(n_0) - g_{\omega K^-}\omega_0(n_0), \tag{3}$$

where available theoretical and experimental analyses constrain U_{K^-} typically from − 50 MeV to − 200 MeV [80–82]. In this work we adopt the representative range of − 100 MeV to − 120 MeV [46,77] to probe its potential impact on gravitational waves. The onset of kaon condensation represents a first-order phase transition, handled with the Gibbs construction (GC) [49,77], see also Refs. [49,74,83,84] for comprehensive discussions. Within this formalism, pressure and chemical potentials continuity across the coexistence phase (CP) are ensured by:

$$P_N(\mu_n, \mu_e) = P_{K^-}(\mu_n, \mu_e) = P_{\rm CP}, \tag{4}$$

while global charge neutrality imposes

$$\chi q_{K^-} + (1-\chi) q_N = 0, \tag{5}$$

where χ is the volume fraction of the kaon meson phase, varying continuously from nucleon phase $\chi = 0$ to kaon phase $\chi = 1$, and q_N and q_{K^-} are the net charge densities within their respective phases. The baryon density and energy density in the CP are therefore expressed as:

$$n_{\rm CP} = \chi n_{K^-} + (1-\chi) n_N, \tag{6}$$

$$\varepsilon_{\rm CP} = \chi \varepsilon_{K^-} + (1-\chi)\varepsilon_N. \tag{7}$$

3 Numerical results and discussions

3.1 Mass–radius relationships and tidal deformability

Evaluating whether the mass–radius relationship satisfies existing astrophysical constraints serves as a fundamental cri-

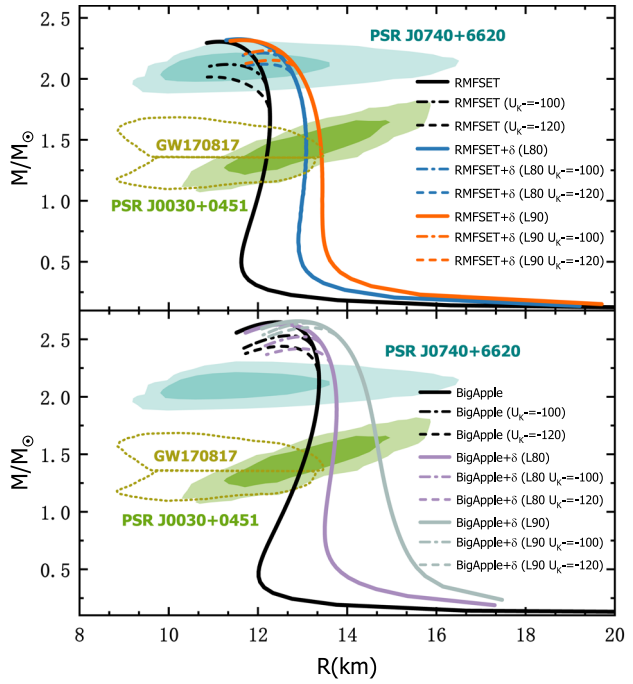

Fig. 1 Upper panel (RMFSET): mass–radius relationship for different symmetry energy slopes of isovector–scalar meson δ and their corresponding kaon condensation NSs with different potential wells, where solid black line marks a pure NS, the dark-blue solid line ($L=80$ MeV) and orange solid line ($L=90$ MeV) respectively represent scenarios considering δ mesons, while the dotted-dashed line ($U_{K^-}=-100$ MeV) and dashed line ($U_{K^-}=-120$ MeV) represent the scenarios of their corresponding NSs with kaon meson condensation. The shaded areas represent the constraints from the PSR J0740+6620 and PSR J0030+0451. The enclosed dotted grey contour indicates the observation imposed by GW170817 event. Lower panel (BigApple): mass–radius relationship for isovector–scalar meson δ under $L=80$ MeV (solid purple line) and $L=90$ MeV (solid dark-green line), and their corresponding kaon condensation NSs with kaon meson potential well $U_{K^-}=-100$ MeV (dotted-dashed line) and $U_{K^-}=-120$ MeV (dashed line)

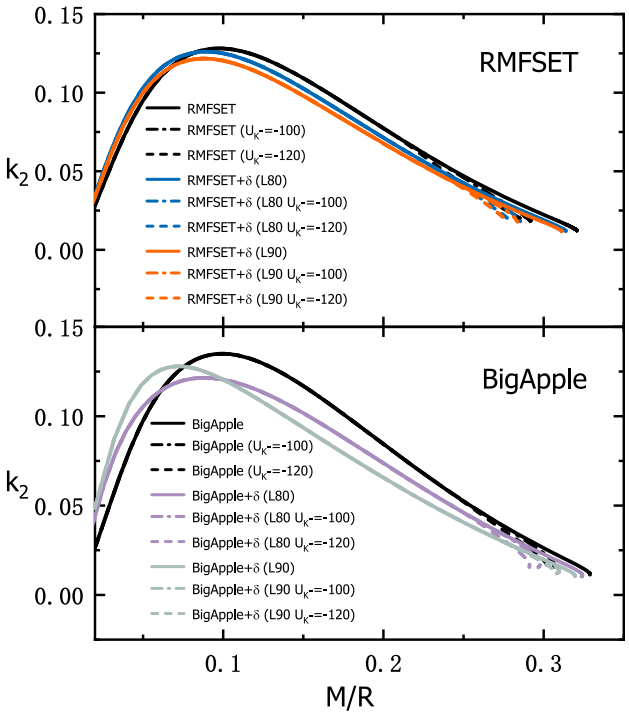

Fig. 2 The tidal Love numbers as a function of the compactness parameter for two classes of relativistic parameter sets. The meanings of the various lines are the same as in Fig. 1

terion for testing any theoretical model or parameter space. Figure 1 displays the mass–radius relationships for NSs with kaon condensation under various δ meson coupling constants. The light shaded regions indicate the observational constraints imposed by the NICER for PSR J0740+6620 and PSR J0030+0451 [7–10], while the enclosed contour dashed lines indicate the constraints imposed by the GW170817 event [16]. In the upper panel, corresponding to the RMFSET set, the standard NS models without δ interactions are represented by solid black lines. The inclusion of δ meson effects at symmetry energy slopes L of 80 MeV and 90 MeV is illustrated by dark-blue and orange solid lines, this effect results in increasingly stiffer EoSs, thereby yielding larger NS radii. Dashed and dotted lines further illustrate NSs with kaon condensation at different potential wells. Since kaon condensation tends to occur at higher densities, it is preferentially realized in more massive NSs, whereas lower-mass stars, particularly around the canonical mass of $1.4M_\odot$ NSs, are less prone to kaon condensation. Moreover, deeper potential wells correspond to more pronounced softening effects. Therefore, considering the combined effects of isovector–scalar mesons and kaon condensation within NSs, we can achieve a configuration with smaller mass and larger radius. For instance, with the RMFSET set, the maximum mass and corresponding radius of a NS can reach $2.31M_\odot$ and 11.15 km, while under conditions of $L=80$ MeV and $U_{K^-}=-100$ MeV, these values shift to $2.12M_\odot$ and 12.26 km. The lower panel illustrates the results using the BigApple set, giving the conclusions similar to those within RMFSET. Moreover, both sets can account for observed $2.0M_\odot$ massive NSs and adequately meet the current observational constraints.

Figures 2 and 3 illustrate from two complementary perspectives how the δ mesons and K^- meson condensation influence tidal effects during the BNS inspiral phase. Figure 2 depicts the tidal Love number k_2 as a function of the compactness parameter $C=M/R$, showing that NSs with smaller C exhibit stronger tidal responses (larger k_2), thus making them more susceptible to distort under their companion star gravitational field. The inclusion of K^- mesons (dashed lines) and δ meson effects (solid lines) both significantly reduce the value of k_2, and this suppression becomes more pronounced with deeper potential wells and larger L values. To facilitate comparison with observational constraints, Fig. 3 presents the observable dimensionless tidal deformability Λ

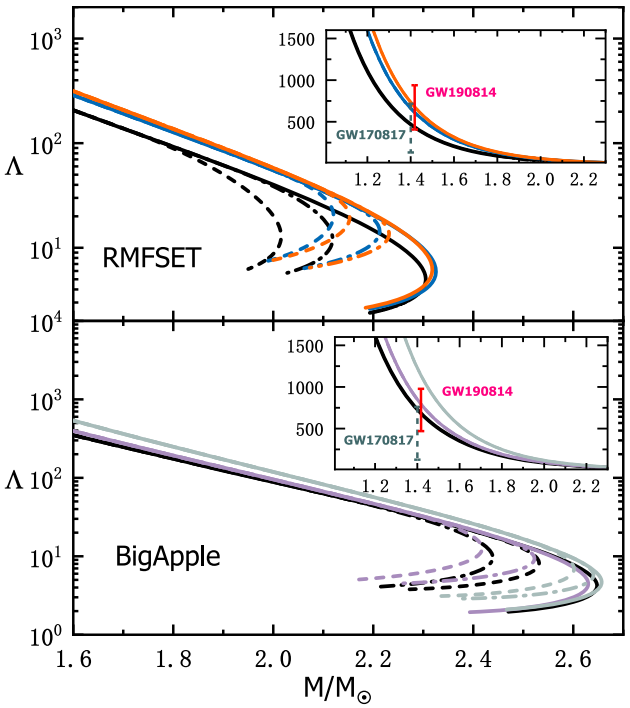

Fig. 3 The dimensionless tidal deformability with NS mass for RMFSET and BigApple scenarios. The subfigure displays the tidal deformability across the entire mass range, with the vertical dashed and solid lines representing the tidal deformability constraints extracted by the gravitational wave events GW170817 and GW190814, respectively

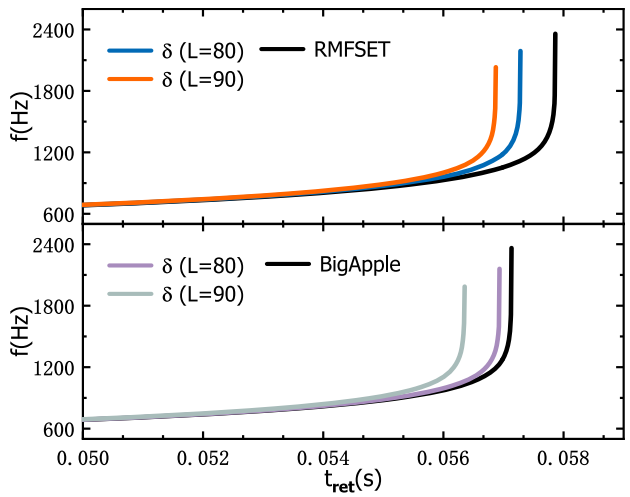

Fig. 4 Upper panel: inspiral gravitational wave frequency f modeled using RMFSET as a function of retarded time for $1.35M_{\odot}$ equal-mass BNS systems with the inclusion of δ meson effects. The different colored curves indicate different cases: standard BNSs (black line), BNSs with δ meson at potentials of $L = 80$ MeV (dark-blue line) and $L = 90$ MeV (orange line), respectively. Lower panel: the gravitational wave frequency for the BigApple scenario

versus NS mass. At a fixed mass, δ mesons yield larger radii (see Fig. 1), thereby lowering C, which facilitate NS distortion under gravitational field and consequently increases tidal deformability Λ. The inset of Fig. 3 highlights observational constraints at $1.4\,M_{\odot}$, where vertical dashed and solid lines denoting tidal deformability intervals inferred from gravitational wave events GW170817 [16] and GW190814 [12], respectively.

From above analysis, although both parameter sets adequately align with current observational constraints, a critical question remains as to whether additional observational channels exist to further distinguish these signals associated with δ mesons and K^- meson condensation? Moving forward, these exotic degrees of freedom are expected to impact gravitational wave properties during BNS inspirals, potentially leaving observable imprints in emitted signals.

3.2 Binary neutron star inspiral gravitational waves

In the search for potential signatures of δ meson and K^- meson within NSs, gravitational waves emitted from binary star mergers have become an indispensable observational tool [85]. Traditional efforts to put constraints on EoSs have relied mainly on bulk stellar observables, such as mass–radius relations [86–89], tidal deformabilities [55,90,91], and gravitational redshifts [92,93]. However, recent detections of BNS and NS-black hole (NSBH) mergers demonstrate that gravitational waves, as a new messengers, carries rich, complementary information capable of markedly tightening constraints on the NS internal structures [94,95]. Our forthcoming analysis aims to investigate the roles of δ mesons and K^- mesons in shaping gravitational wave signals during the inspiral phase, and tries to seek the potential imprints they may leave.

A BNS coalescence inherently proceeds through three distinct stages of inspiral, merger and ringdown [85]. Among these, the inspiral phase, characterized by relatively low velocities and weak gravitational fields, is effectively described through the Post-Newtonian (PN) approximation [60,96–98]. As a systematic expansion of general relativity, the PN approximation method has undergone rigorous validation and demonstrates exceptional precision in modeling inspiral gravitational wave signals [99,100]. A detailed derivation of the PN approximation method can be found in Appendix or our previous work [61], for more comprehensive discussions, readers are referred to Refs. [96,97,101,101–105].

To investigate the influence of δ meson effects on gravitational wave properties during the inspiral phase, Fig. 4 shows gravitational wave frequency as a function of retarded time during the inspiral phase for two parameter sets with a typical equal-mass BNS inspiral system of $1.35M_{\odot}$. For the RMFSET (upper panel), we compare BNS systems of δ mesons at different Ls with standard BNS systems. From the viewpoint of retarded inspiral time, the impact of δ meson accelerates the inspiral process, resulting in shorter retarded times com-

Table 2 Gravitational wave frequencies and retarded times during BNS inspiral phase in the RMFSET and BigApple sets. Upper panel presents results for $1.35M_{\odot}$ equal-mass standard BNS systems and corresponding BNS systems incorporating the δ meson effects at different symmetry energy slopes. Lower panel shows the BNS systems under δ meson effects for maximum equal-mass kaon meson condensation BNSs at different kaon meson potential wells

CASE		$f_{\max}$ (Hz)	$t_{\rm ret}$(s)
RMFSET	Standard BNS	2365.32	0.05786
	BNS + $\delta(L$ 80)	2191.80	0.05728
	BNS + $\delta(L$ 90)	2041.07	0.05685
BigApple	Standard BNS	2384.27	0.05714
	BNS + $\delta(L$ 80)	2167.13	0.05692
	BNS + $\delta(L$ 90)	1985.11	0.05635
RMFSET (δ)	BNS (δ)	2169.05	0.10357
	BNS (δ) + $U_{\rm K^-}(-100)$	1917.95	0.09503
	BNS (δ) + $U_{\rm K^-}(-120)$	1889.33	0.08975
BigApple (δ)	BNS (δ)	1914.18	0.11905
	BNS (δ) + $U_{\rm K^-}(-100)$	1707.89	0.11373
	BNS (δ) + $U_{\rm K^-}(-120)$	1690.42	0.10942

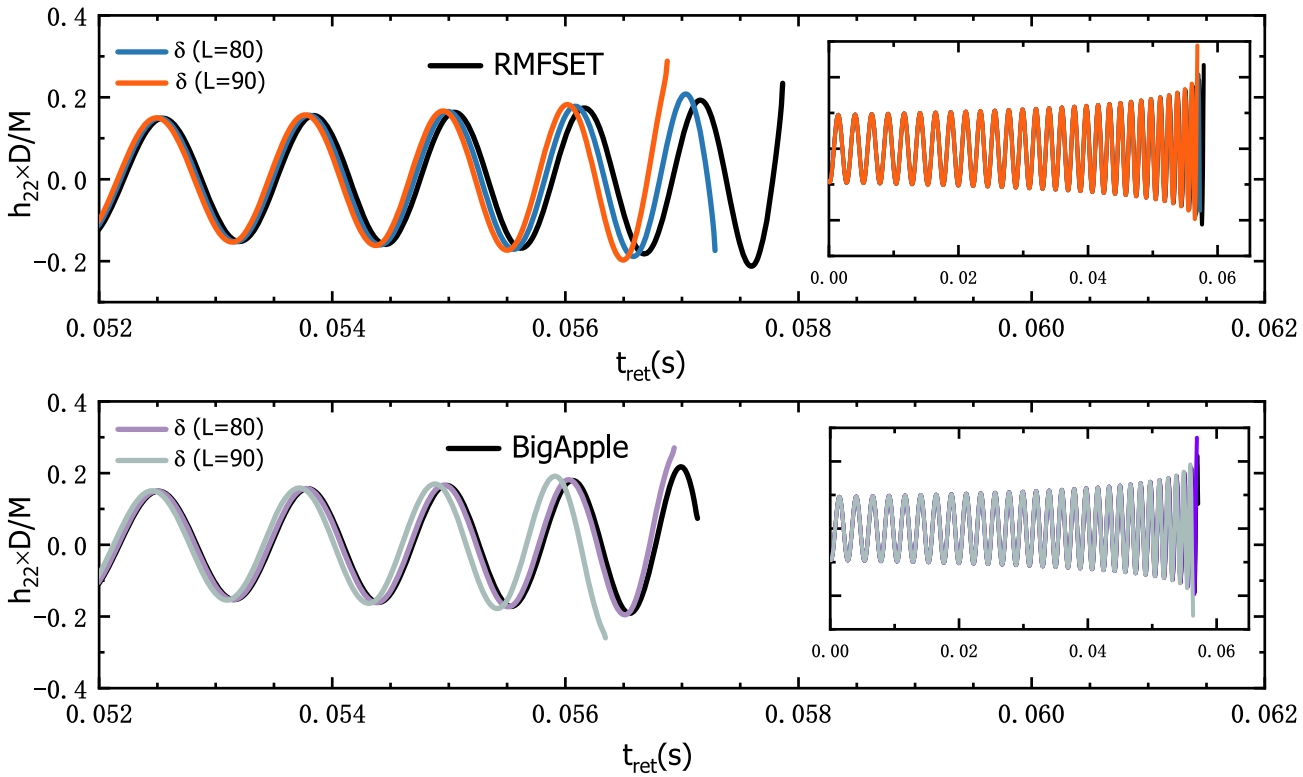

Fig. 5 Within the RMFSET (upper panel) and BigApple (lower panel) parameter sets that include δ mesons, the gravitational wave amplitude h_{22} as a function of retarded time $t_{\rm ret}$ for $1.35M_{\odot}$ equal-mass BNS systems across various symmetry energy slopes, where the different colored curves represent the respective scenarios illustrated in Fig. 4

pared to standard BNS. Specifically, $L = 90$ MeV yields the shortest inspiral time of approximately 0.05685s, $L = 80$ MeV yields 0.05728s, while the standard BNS system has a relatively longer retarded inspiral time of about 0.05786s.

Furthermore, gravitational wave frequency f increases continuously during inspiral stage and peaks in the final stage. The δ meson effects reduce the maximum gravitational wave frequencies at the final inspiral stage compared to standard BNS. The maximum frequency is approximately 2041.07Hz for $L = 90$ MeV (orange solid line), 2191.80 Hz for $L = 80$ MeV (dark blue solid line), and 2365.32 Hz for standard BNS (black solid line). These differences can be inferred from Figs. 1 and 3, as the inspiral dynamics are highly sensitive to NS tidal effects. Since the presence of δ meson increases the NS radius (see Fig. 1), which facilitates tidal deformability and thus accelerates the inspiral, conse-

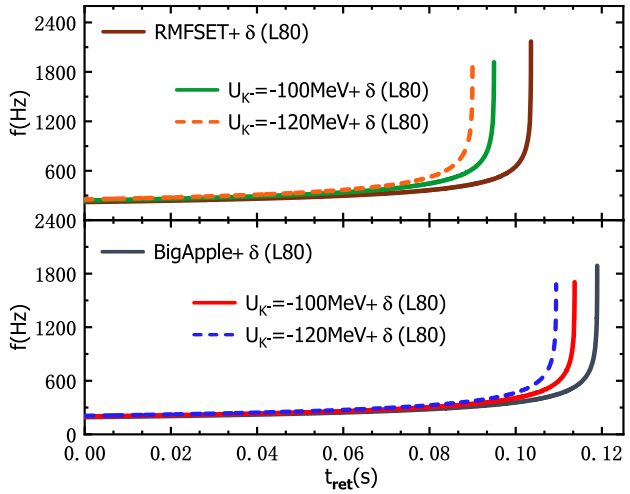

Fig. 6 Upper panel (RMFSET): inspiral gravitational wave frequency f as a function of retarded time $t_{\rm ret}$ for maximum equal-mass kaon meson condensation BNS systems incorporating the δ mesons under symmetry energy slope $L = 80$ MeV. The different colored curves mark different cases: BNSs (brown solid line), BNSs with kaon condensation at potentials of $U_{K^-} = -100$ MeV (green solid line) and $U_{K^-} = -120$ MeV (orange dash line), respectively. Lower panel (BigApple): Gravitational wave frequency for the BigApple scenario

quently emitting lower gravitational wave frequency. Similar conclusions are observed for the BigApple parameter set, showing that δ mesons accelerate inspiral processes, leading to shorter retarded times and lower gravitational wave frequencies. Detailed numerical results of gravitational wave properties for both parameter sets are summarized in the upper panel of Table 2.

Beyond the analyses from frequency and retarded time, we further examine δ meson impacts through gravitational waveforms. Figure 5 compares the dominant ($l = 2, m = 2$) mode [106–108] gravitational wave strain amplitude between δ meson BNS system and standard BNS system for both parameter sets. The inset displays full inspiral waveforms under PN approximation, showing amplitude growth reach their maximum values at the final stage. Due to the δ meson-induced shortening of retarded time (see Fig. 4), there is a notable phase shifts in gravitational waveforms, resulting in asynchronous waveform pattern compared to standard BNS system.

To demonstrate the impact of δ mesons on BNS systems with kaon condensation, we fix the symmetry energy slope L at 80 MeV in subsequent analyses. Given that kaons appear predominantly in massive NS interiors (see Fig. 1), our study concentrates on evaluating the maximum equal-mass BNS inspiral phase under different kaon potential wells with incorporating δ meson interactions, exploring corresponding gravitational wave frequency, retarded time, and waveforms. Figure 6 illustrates the dependence of gravitational wave frequency on the inspiral retarded time, with the upper panel showing RMFSET and the lower panel BigApple scenarios. Both parameter sets reveal that deeper kaon potential wells correlate with shorter inspiral retarded times and lower gravitational wave frequencies compared to BNS system involving only δ mesons. Numerical results are detailed in the lower panel of Table 2. Notably, with the δ meson effects in BNS systems, the RMFSET predicts a maximum inspiral gravitational wave frequency $f_{\rm max}$ of 2169.05 Hz, while the inclusion of K^- meson condensation further reduces the frequency $f_{\rm max}$ to approximately 1900 Hz (1917.95 Hz for $U_{K^-}(-100)$ and 1889.33 Hz for $U_{K^-}(-120)$), corresponding to a reduction of $\Delta f_{\rm max} \simeq 200$ Hz, i.e. a relative change of about 9-13% at the end of the inspiral. For the BigApple (δ) models, the frequency $f_{\rm max}$ changes from 1914.18 Hz to 1707.89 Hz for $U_{K^-}(-100)$ MeV and 1690.42 Hz for $U_{K^-}(-120)$ MeV, again a relative reduction of 11∼12%. In the time domain, these models also show that deeper kaon potentials shorten the inspiral retarded time by about 5 ms compared to the case without kaons, whereas varying only the isovector–scalar meson couplings leads to changes at the level of 1 ms.

From an observational standpoint, the relevant frequency shifts occur close to merger, in the kHz band. Their detectability therefore depends primarily on the high frequency strain sensitivity and on the total signal-to-noise ratios. While current LIGO-Virgo-KAGRA detectors typically accumulate only modest signal-to-noise ratio above 1 kHz for the GW170817-like events, the third-generation instruments such as the Einstein Telescope (ET) [109–112] and the Cosmic Explorer (CE) [112] are expected to provide substantially improved sensitivity in the 1-3 kHz range, together with much larger network signal-to-noise ratios for BNS mergers [85,113]. A simple order-of-magnitude estimate can be obtained by treating the characteristic frequency $f_{\rm max}$ as a parameter inferred from the last 20–30 ms. In a Fisher-matrix approximation [114–117], the corresponding statistical uncertainty scales as $\sigma_{f_{\rm max}} \propto (T_{\rm eff}\rho_{\rm snr})^{-1}$, where $T_{\rm eff}$ is the effective duration over which the high-frequency signal contributes, and $\rho_{\rm snr}$ is the signal-to-noise ratio accumulated in the kHz band. For $T_{\rm eff} \sim$ 20–30 ms and $\rho_{\rm snr} \sim$ 10-20, one expects $\sigma_{f_{\rm max}}$ of order a few Hz. Consequently, a systematic shift of $\Delta f_{\rm max} \simeq 200$ Hz between models with and without kaon condensation corresponds to isovector–scalar meson effect once $\rho_{\rm snr} \geq$ 20–30. For second-generation detectors, such high signal-to-noise ratio in the kHz band will only be achieved for very nearby and rare events, whereas forthcoming third-generation detectors ET and CE are expected to reach network signal-to-noise ratio ≥ 100 for typical BNS mergers, making $\sigma_{f_{\rm max}}$ well below $\mathcal{O}(50{\rm Hz})$ and thus allowing a robust discrimination between models with and without kaon condensation in favorable cases.

Figure 7 displays the evolution of the dominant mode gravitational wave strain h_{22} during inspiral phase, with insets

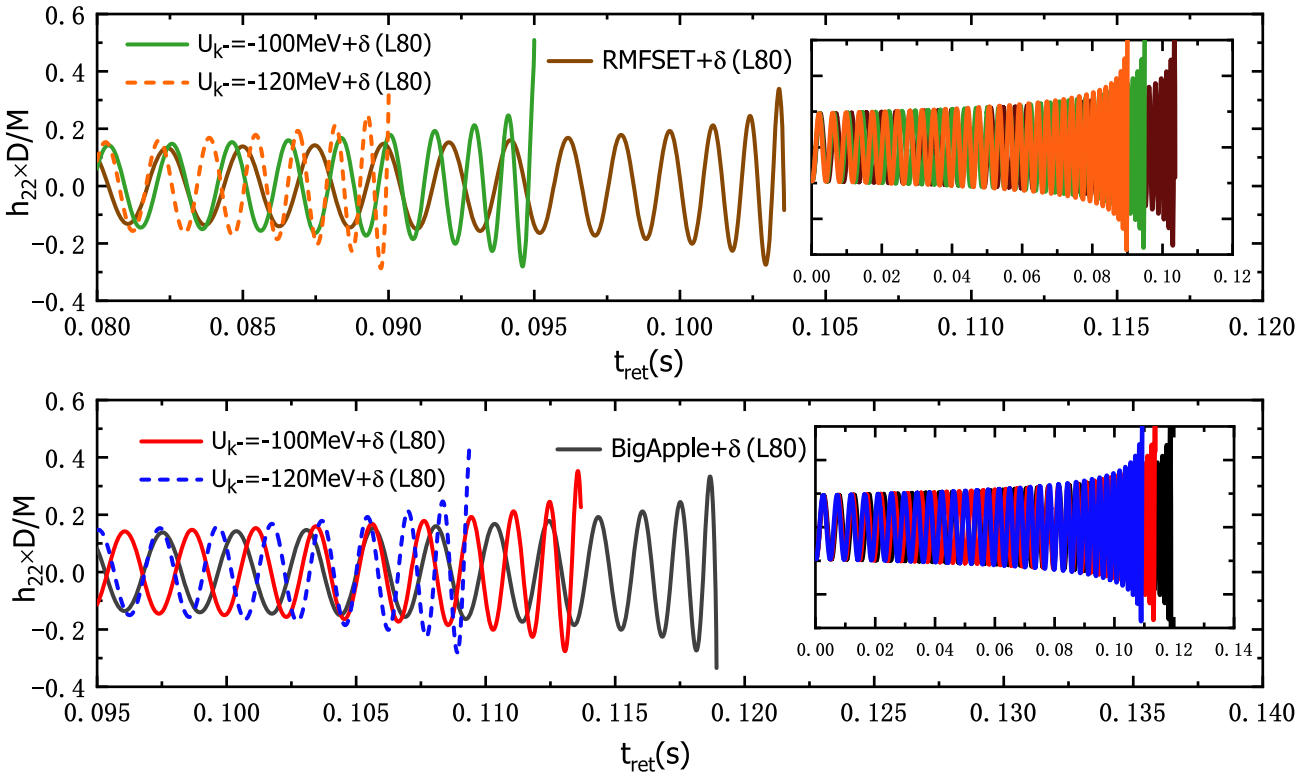

Fig. 7 Within the RMFSET (upper panel) and BigApple (lower panel) parameter sets that include δ meson effects, the gravitational wave amplitude h_{22} as a function of retarded time $t_{\rm ret}$ for BNS systems with maximum kaon meson condensation across various kaon meson potential wells, where the different colored curves represent the respective scenarios illustrated in Fig. 6

showing entire inspiral waveforms. As inspiral stage proceeds, phase deviations among various kaon potential wells become increasingly pronounced, reaching maximum amplitude and phase shift in the final stage, after which PN approximations break down and numerical relativity simulations take over [85]. Figure 7 clearly indicates that kaon meson condensation accelerates inspiral phase, yielding shorter duration and lower frequency (as shown in Fig. 6). This acceleration occurs because kaon meson condensation softens the EoS, facilitating tidal effects and thus accelerating inspiral dynamics meanwhile emitting lower frequency gravitational waves.

Intriguingly, unlike δ meson effects that predominantly influencing 1.4 $M_\odot$ NSs, kaon effects appear in massive NSs. Figures 6 and 7 demonstrate that BNS system with kaon condensation exhibit significantly shorter retarded times than those influenced solely by δ mesons. Moreover, retarded time differences among kaon meson potentials are more pronounced. Specifically, for the RMFSET, the retarded time without kaon effects is 0.10357 s, compared to 0.09503 s at $U_{K^-} = -100$ MeV, and 0.08975 s at $U_{K^-} = -120$ MeV, corresponding to five milliseconds difference. Comparable five milliseconds variations are also observed in the BigApple. In contrast, δ meson-induced retarded time variations characterized by symmetry energy slopes are limited to about one millisecond (see Figs. 4, 5 and Table 2).

To assess whether the trends reported above persist beyond a single canonical mass configuration, we extend our post-Newtonian inspiral calculations to a sequence of equal-mass BNS systems spanning a range of chirp mass $\mathscr{M}_c$

$$\mathscr{M}_c = \frac{(M_1 M_2)^{3/5}}{(M_1 + M_2)^{1/5}}, \tag{8}$$

focusing on the cases that incorporate isoscalar-vector meson interactions. For consistency with our previous discussion we extend a component mass $1.6M_\odot$ equal-mass BNS with $\mathscr{M}_c = 1.392M_\odot$, a $1.8M_\odot$ equal-mass BNS with $\mathscr{M}_c = 1.566M_\odot$, and a $2.0M_\odot$ equal-mass BNS with $\mathscr{M}_c = 1.741M_\odot$. The resulting trends are summarized in Table 3 for both the RMFSET and BigApple parameter sets. At fixed chirp mass, the inclusion of the isoscalar-vector meson systematically shortens the merger retarded time and lowers the maximum inspiral frequency with respect to the corresponding standard BNS models. Importantly, the relative reduction in $f_{\rm max}$ at order $\sim$10% level persists across the explored chirp mass range, and the frequency difference remains approximately at the $\mathscr{O}(200)$ Hz and the shortening of retarded time remains at the level of a few milliseconds. Regarding kaon

Table 3 Gravitational wave frequencies and retarded times during BNS inspiral phase in the RMFSET and BigApple sets. **CASE** presents results for equal-mass standard BNS systems and their corresponding BNS systems incorporating the δ meson effects at different symmetry energy slopes and different chirp masses $\mathscr{M}_c$ (a $1.35M_\odot$ equal-mass standard BNS model with $\mathscr{M}_c = 1.175M_\odot$, a $1.6M_\odot$ equal-mass BNS with $\mathscr{M}_c = 1.392M_\odot$, a $1.8M_\odot$ equal-mass BNS with $\mathscr{M}_c = 1.566M_\odot$ and a $2.0M_\odot$ equal-mass BNS with $\mathscr{M}_c = 1.741M_\odot$)

CASE		$\mathscr{M}_c = 1.175M_\odot$		$\mathscr{M}_c = 1.392M_\odot$		$\mathscr{M}_c = 1.566M_\odot$		$\mathscr{M}_c = 1.741M_\odot$	
		$f_{\max}$ (Hz)	$t_{\rm ret}$(s)	$f_{\max}$ (Hz)	$t_{\rm ret}$(s)	$f_{\max}$ (Hz)	$t_{\rm ret}$(s)	$f_{\max}$(Hz)	$t_{\rm ret}$(s)
RMFSET	Standard BNS	2365.32	0.05786	2455.88	0.07021	2510.42	0.07978	2672.47	0.08924
	BNS + $\delta(L\ 80)$	2191.80	0.05728	2271.41	0.06997	2335.13	0.07956	2474.93	0.08912
	BNS + $\delta(L\ 90)$	2041.07	0.05685	2163.33	0.06979	2221.78	0.07947	2362.99	0.08905
BigApple	Standard BNS	2384.27	0.05714	2480.34	0.06964	2534.85	0.07925	2681.49	0.08883
	BNS + $\delta(L\ 80)$	2167.13	0.05692	2257.76	0.06958	2349.68	0.07913	2436.12	0.08873
	BNS + $\delta(L\ 90)$	1985.11	0.05635	2105.28	0.06898	2185.18	0.07891	2282.72	0.08854

condensation, we note that it typically appear only in sufficiently massive NS interiors (see Fig. 1). As a consequence, it is not always straightforward to extend a one-to-one comparison of kaon effects across the entire chirp mass sequence considered here, particularly at the lower mass cases where the central density may remain below the onset threshold. Nevertheless, this limitation does not affect our main conclusion regarding the role of kaon condensation in modulating the gravitational wave signal that its presence further reduces the retarded time and shifts the maximum inspiral frequency to lower values. These $\mathscr{M}_c$ dependent results presented here are intended to demonstrate a physically motivated trend rather than a unique signature from a single event. A systematic exploitation of $t_{\rm ret}(\mathscr{M}_c)$ and $f_{\max}(\mathscr{M}_c)$ is most naturally pursued in hierarchical bayesian analyses combining multiple BNS events, which lies beyond the scope of the present work. Our calculations nevertheless provide a useful baseline for future studies.

Jointly analyzing these signal differences with constraints from the mass–radius relation and tidal deformability will better enable the search for potential δ mesons and K^- condensation signals in NSs, it will also help us gain deeper insights into NS internal structure. Although these differences are relatively small, the upcoming improvements in sensitivity from the upgraded LIGO–Virgo/KAGRA network [109,118] and A+ upgrades [118], especially from third-generation gravitational wave detectors [109–112,112], will enable precise discrimination of potential K^- meson condensation effects and δ meson signals in NSs. These advancements will not only allow for tighter constraints on the EoS through inspiral phase gravitational wave analysis, but also significantly broaden the utility of gravitational waves as a powerful probe of NS structure.

4 Summary

In this study, we conduct a self-consistent exploration of isovector–scalar mesons and kaon condensation in NS interiors under an extended nonlinear RMF model within two widely employed parameter sets, RMFSET [69] and BigApple [65]. Our analysis aims to quantify their influence on the gravitational wave characteristic signatures during the BNS inspiral phase, and try to estimate how these distinctive signals can be leveraged to probe NS internal structure. During the BNS inspiral phase, we analysis the differences from viewpoint of inspiral retarded time and gravitational wave frequency. The impact of δ mesons accelerates the inspiral process, resulting in shorter retarded times and reduce maximum inspiral gravitational wave frequencies compared to standard BNS systems. We have further shown that, for both parameter sets, the retarded time and maximum inspiral frequency exhibit a coherent dependence on the binary chirp mass, and for a given $\mathscr{M}_c$ the presence of δ mesons shortens the retarded time and shifts the maximum frequency to lower values. Notably, binary systems with kaon condensation exhibit even shorter inspiral times and lower frequencies compared to systems influenced solely by δ mesons. Both parameter sets reveal that retarded time differences among kaon meson potentials are approximately five milliseconds, whereas δ meson-induced retarded time variations are around one millisecond. Moreover, the inclusion of kaon meson condensation systematically lowers the maximum inspiral gravitational wave frequency by around 200 Hz, while also shortening the inspiral retarded time by about 5 ms relative to the case with only isovector–scalar mesons. These differences occur in the high-frequency (kHz) regime that lies within the sensitive band of third-generation gravitational wave detectors like ET and CE. As discussed in Sect. 3.2, simple signal-to-noise ratio estimates indicate that such $\mathscr{O}$(200Hz) frequency shifts are unlikely to be robustly resolved with current LIGO–Virgo–KAGRA detectors for typical BNS events, but may become measurable for high signal-to-noise ratio

BNS mergers observed by future facilities. At the same time, our results for the shifts in retarded times and maximum inspiral frequencies induced by isoscalar-vector δ mesons and kaon condensation are intended to demonstrate a physically motivated trend rather than a unique signature from a single event. A systematic exploitation of $t_{\rm ret}(\mathscr{M}_c)$ and $f_{\rm max}(\mathscr{M}_c)$ within hierarchical bayesian analyses combining multiple BNS events will be the most promising avenue for constraining the strength of the isovector–scalar channel and the kaon optical potential. Combined with observable mass–radius relationships and tidal deformabilities, our findings therefore suggest that inspiral gravitational wave signals may potentially provide an effective tool for identifying possible imprints of isovector–scalar meson effects and kaon meson condensation in NS cores, and also could offer precise constraints on both δ meson coupling strengths and K^- optical potential depths from gravitational wave inspiral phase. Future studies will extend RMF framework to numerical relativity merger simulations and include hyperon and quark degrees of freedom, thereby paving the way toward a effective explore of dense matter.

Acknowledgements This work is supported by the National Natural Science Foundation of China (no. 12405163, no. 12535009, no. 12035011) and National Key R&D Program of China (no. 2023YFA1606503)

Data Availability Statement This manuscript has no associated data. [Author's' comment: Data sharing not applicable to this article as no datasets were generated or analysed during the current study.]

Code Availability Statement This manuscript has no associated code/software. [Author's comment: Code/Software sharing not applicable to this article as no code/software was generated or analysed during the current study.]

Funded by SCOAP[3].

Appendix: Post-Newtonian approximation in binary star inspiral phase gravitational waves

In quasicircular binaries emitting gravitational waves, the radiative energy luminosity $\mathscr{L}$ balances the change in orbital energy E according to

$$\mathscr{L} = -\frac{dE}{dt} = -\frac{dE/dx}{dt/dx}, \tag{9}$$

with x being the gauge-invariant PN expansion parameter defined by $x = \left(M_{\rm tot}\frac{{\rm d}\Phi}{{\rm d}t}\right)^{2/3} = (M_{\rm tot}\Omega)^{2/3}$, where $M_{\rm tot}$ denotes the total mass of the system, Φ the orbital phase, and Ω the orbital angular frequency. For a quasicircular binary with $M_{\rm tot} = M_1 + M_2$ and angular velocity Ω, the 3.5PN approximation to the orbital energy reads [96,101,102]:

$$\begin{aligned} E = -\frac{M_{\rm tot}\eta x}{2}\Bigg\{1 &+ \left(-\frac{3}{4} - \frac{\eta}{12}\right)x + \left(-\frac{27}{8} + \frac{19\eta}{8} - \frac{\eta^2}{24}\right)x^2 \\ &+ \left[-\frac{675}{64} + \left(\frac{34445}{576} - \frac{205\pi^2}{96}\right)\eta - \frac{155\eta^2}{96} - \frac{35\eta^3}{5184}\right]x^3\Bigg\}, \end{aligned} \tag{10}$$

with $\eta = m_1 m_2/M_{\rm tot}^2$ the symmetric mass ratio. At the same PN order, the gravitational wave luminosity $\mathscr{L}$ can be written as [97,101,101,119]:

$$\begin{aligned} \mathscr{L} = \frac{32\eta^2 x^5}{5}\Bigg\{1 &+ \left(-\frac{1247}{336} - \frac{35\eta}{12}\right)x + 4\pi x^{3/2} \\ &+ \left[\frac{6643739519}{69854400} + \frac{16\pi^2}{3} - \frac{1712\gamma_E}{105} - \frac{856}{105}\ln(16x) \right. \\ &\left. + \left(-\frac{134543}{7776} + \frac{41\pi^2}{48}\right)\eta - \frac{94403\eta^2}{3024} - \frac{775\eta^3}{324}\right]x^3 \\ &+ \left(-\frac{16285}{504} + \frac{214745\eta}{1728} + \frac{193385\eta^2}{3024}\right)\pi x^{7/2} \\ &+ \left(-\frac{44711}{9072} + \frac{9271\eta}{504} + \frac{65\eta^2}{18}\right)x^2 \\ &+ \left(-\frac{8191}{672} - \frac{583\eta}{24}\right)\pi x^{5/2}\Bigg\}, \end{aligned} \tag{11}$$

with $\gamma_E \approx 0.5772$ the Euler–Mascheroni constant. The dominant spherical-harmonic mode of the strain, $(\ell, m) = (2, 2)$, constructed from spin-weighted harmonics, is given by [106–108]:

$$\begin{aligned} h_{22} = -8\sqrt{\frac{\pi}{5}}\frac{M_{\rm tot}\eta}{D}e^{-2i\phi}x\Bigg\{1 &+ \left(-\frac{107}{42} + \frac{55\eta}{42}\right)x \\ &+ \left[\frac{27027409}{646800} - \frac{856\gamma_E}{105} + \frac{2\pi^2}{3} + \frac{428i\pi}{105} - \frac{428}{105}\ln(16x) \right. \\ &\left. + \left(\frac{41\pi^2}{96} - \frac{278185}{33264}\right)\eta - \frac{20261\eta^2}{2772} + \frac{114635\eta^3}{99792}\right]x^3 \\ &+ \left(-\frac{2173}{1512} - \frac{1069\eta}{216} + \frac{2047\eta^2}{1512}\right)x^2 + 2\pi x^{3/2} \\ &+ \left[-\frac{107\pi}{21} + \left(\frac{34\pi}{21} - 24i\right)\eta\right]x^{5/2}\Bigg\}, \end{aligned} \tag{12}$$

where D is the source distance, taken to be 100 Mpc in our calculations. The orbital phase Φ evolves according to

$$\frac{dx}{dt} = -\frac{\mathscr{L}}{dE/dx}, \tag{13}$$

$$\frac{d\Phi}{dt} = \frac{x^{3/2}}{M}, \tag{14}$$

and we employ the TaylorT4 scheme to integrate them. Although formally appearing at 5PN order, tidal interactions significantly affect the inspiral process and must therefore be incorporated. Including these contributions yields [103–105]:

$$\frac{\mathrm{d}x}{\mathrm{d}t} = \frac{64\eta}{5M_{\rm tot}} x^5 \left\{ F^{\rm T4}_{3.5}(x) + F^{\rm T4}_{\rm Tidal}(x) \right\}, \tag{15}$$

where $F^{\rm T4}_{3.5}(x)$ within the TaylorT4 scheme gives as

$$\begin{aligned} F^{\rm T4}_{3.5}(x) = 1 &- \left(\frac{743}{336} + \frac{11}{4}\eta\right) x + 4\pi x^{3/2} + \left(\frac{34103}{18144} \right. \\ &\left. + \frac{13661}{2016}\eta + \frac{59}{18}\eta^2\right) x^2 - \left(\frac{4159}{672} + \frac{189}{8}\eta\right)\pi x^{5/2} \\ &+ \left[\frac{16447322263}{139708800} - \frac{1712}{105}\gamma_E - \frac{56198689}{217728}\eta \right. \\ &+ \frac{541}{896}\eta^2 - \frac{5605}{2592}\eta^3 + \frac{\pi^2}{48}(256 + 451\eta) \\ &\left. - \frac{856}{105}\ln(16x)\right] x^3 + \left(-\frac{4415}{4032} \right. \\ &\left. + \frac{358675}{6048}\eta + \frac{91495}{1512}\eta^2\right)\pi x^{7/2}. \end{aligned} \tag{16}$$

The term $F^{\rm T4}_{\rm Tidal}(x)$ accounts for tidal-related corrections, and following Vines [120], the 1PN-accurate expression is

$$\begin{aligned} F^{\rm T4}_{\rm Tidal}(x) = \frac{32\chi_1\lambda_2}{5M^6_{\rm tot}} &\left[12\,(1+11\chi_1)\,x^{10} + \left(\frac{4421}{28} - \frac{12263}{28}\chi_2 \right.\right. \\ &\left.\left. + \frac{1893}{2}\chi_2^2 - 661\chi_2^3\right) x^{11}\right] + (1 \leftrightarrow 2), \end{aligned}$$

where $\chi_1 = M_1/M_{\rm tot}$ and $\chi_2 = M_2/M_{\rm tot}$ are the mass fractions, and λ_1, λ_2 the corresponding tidal deformabilities. For equal-mass binaries this reduces to [104]:

$$F^{\rm T4}_{\rm Tidal}(x) = \frac{52}{5M_{\rm tot}}\frac{k_2}{C^5} x^{10}\left(1 + \frac{5203}{4368}x\right), \tag{17}$$

with k_2 the tidal Love number and C the stellar compactness. In this study, we consider a representative equal-mass binary NS system. The integration begins at $f = 371$ Hz, i.e. $M_{\rm tot}\Omega_0 = 0.0155$. The source is observed at the retarded time $t_{\rm ret} = t - r_*$, where r_* is the tortoise coordinate, expressed by [104]

$$r_* = r_A + 2M_{\rm tot}\ln\left(\frac{r_A}{2M_{\rm tot}} - 1\right), \tag{18}$$

with $r_{\rm A} = \sqrt{A/4\pi}$ and A the proper area of a spherical surface.

References

1. J.M. Lattimer, M. Prakash, The physics of neutron stars. Science **304**(5670), 536–542 (2004). https://doi.org/10.1126/science.1090720
2. M. Oertel, M. Hempel, T. Klähn, S. Typel, Equations of state for supernovae and compact stars. Rev. Mod. Phys. **89**, 015007 (2017). https://doi.org/10.1103/RevModPhys.89.015007
3. G. Burgio, H.-J. Schulze, I. Vidaña, J.-B. Wei, Neutron stars and the nuclear equation of state. Prog. Part. Nucl. Phys. **120**, 103879 (2021). https://doi.org/10.1016/j.ppnp.2021.103879
4. P.B. Demorest, T. Pennucci, S.M. Ransom et al., A two-solar-mass neutron star measured using Shapiro delay. Nature **467**(7319), 1081–1083 (2010). https://doi.org/10.1038/nature09466
5. E. Fonseca, T.T. Pennucci, J.A. Ellis et al., The NANOGRAV nine-year data set: mass and geometric measurements of binary millisecond pulsars. Astrophys. J. **832**(2), 167 (2016). https://doi.org/10.3847/0004-637X/832/2/167
6. J. Antoniadis, P.C.C. Freire, N. Wex et al., A massive pulsar in a compact relativistic binary. Science **340**(6131), 448 (2013)
7. M.C. Miller, F.K. Lamb, A.J. Dittmann et al., PSR J0030+0451 mass and radius from NICER data and implications for the properties of neutron star matter. Astrophys. J. **887**(1), L24 (2019). https://doi.org/10.3847/2041-8213/ab50c5
8. T.E. Riley, A.L. Watts, S. Bogdanov et al., A NICER view of PSR J0030+0451: millisecond pulsar parameter estimation. Astrophys. J. **887**(1), L21 (2019). https://doi.org/10.3847/2041-8213/ab481c
9. M.C. Miller, F.K. Lamb, A.J. Dittmann et al., The radius of PSR J0740+6620 from NICER and XMM-newton data. Astrophys. J. Lett. **918**(2), L28 (2021). https://doi.org/10.3847/2041-8213/ac089b
10. T.E. Riley, A.L. Watts, P.S. Ray et al., A NICER view of the massive pulsar PSR J0740+6620 informed by radio timing and XMM-Newton spectroscopy. Astrophys. J. Lett. **918**(2), L27 (2021). https://doi.org/10.3847/2041-8213/ac0a81
11. D. Choudhury, T. Salmi, S. Vinciguerra et al., A NICER view of the nearest and brightest millisecond pulsar: PSR J0437–4715. Astrophys. J. Lett. **971**(1), L20 (2024). https://doi.org/10.3847/2041-8213/ad5a6f
12. R. Abbott, T.D. Abbott, S. Abraham et al., GW190814: gravitational waves from the coalescence of a 23 solar mass black hole with a 2.6 solar mass compact object. Astrophys. J. **896**(2), L44 (2020). https://doi.org/10.3847/2041-8213/ab960f
13. R.W. Romani, D. Kandel, A.V. Filippenko, T.G. Brink, W. Zheng, PSR J0952–0607: the fastest and heaviest known galactic neutron star. Astrophys. J. Lett. **934**(2), L17 (2022). https://doi.org/10.3847/2041-8213/ac8007
14. V. Doroshenko, V. Suleimanov, G. Pühlhofer, A. Santangelo, A strangely light neutron star within a supernova remnant. Nat. Astron. **6**(12), 1444–1451 (2022). https://doi.org/10.1038/s41550-022-01800-1
15. B. Müller, A. Heger, J. Powell, Minimum neutron star mass in neutrino-driven supernova explosions. Phys. Rev. Lett. **134**, 071403 (2025). https://doi.org/10.1103/PhysRevLett.134.071403
16. B.P. Abbott, R. Abbott, T.D. Abbott et al., GW170817: observation of gravitational waves from a binary neutron star Inspiral. Phys. Rev. Lett. **119**, 161101 (2017). https://doi.org/10.1103/PhysRevLett.119.161101

17. S. Gandolfi, A. Gezerlis, J. Carlson, Neutron matter from low to high density. Annu. Rev. Nucl. Part. Sci. **65**, 303–328 (2015). https://doi.org/10.1146/annurev-nucl-102014-021957
18. K. Hebeler, J. Holt, J. Menéndez, A. Schwenk, Nuclear forces and their impact on neutron-rich nuclei and neutron-rich matter. Annu. Rev. Nucl. Part. Sci. **65**, 457–484 (2015). https://doi.org/10.1146/annurev-nucl-102313-025446
19. J. Walecka, A theory of highly condensed matter. Ann. Phys. **83**(2), 491–529 (1974). https://doi.org/10.1016/0003-4916(74)90208-5
20. B.D. Serot, Quantum hadrodynamics. Rep. Prog. Phys. **55**(11), 1855 (1992). https://doi.org/10.1088/0034-4885/55/11/001
21. P. Ring, Relativistic mean field theory in finite nuclei. Prog. Part. Nucl. Phys. **37**, 193–263 (1996). https://doi.org/10.1016/0146-6410(96)00054-3
22. N.K. Glendenning, The hyperon composition of neutron stars. Phys. Lett. B **114**(6), 392–396 (1982). https://doi.org/10.1016/0370-2693(82)90078-8
23. H. Shen, H. Toki, K. Oyamatsu et al., Relativistic equation of state of nuclear matter for supernova and neutron star. Nucl. Phys. A **637**(3), 435–450 (1998). https://doi.org/10.1016/S0375-9474(98)00236-X
24. I. Bednarek, R. Manka, Structure and properties of neutron stars in the relativistic mean-field theory. Int. J. Mod. Phys. D **10**(05), 607–624 (2001). https://doi.org/10.1142/S0218271801001104
25. F.J. Fattoyev, C.J. Horowitz, J. Piekarewicz, G. Shen, Relativistic effective interaction for nuclei, giant resonances, and neutron stars. Phys. Rev. C **82**, 055803 (2010). https://doi.org/10.1103/PhysRevC.82.055803
26. V. Parmar, H.C. Das, M.K. Sharma, S.K. Patra, Magnetized neutron star crust within effective relativistic mean-field model. Phys. Rev. D **107**, 043022 (2023). https://doi.org/10.1103/PhysRevD.107.043022
27. S. Yang, D. Wen, Systematic correlation analysis between the nuclear matter parameters and neutron star properties within relativistic mean-field theory. Phys. Rev. D **107**, 063009 (2023). https://doi.org/10.1103/PhysRevD.107.063009
28. H. Müller, B.D. Serot, Relativistic mean-field theory and the high-density nuclear equation of state. Nucl. Phys. A **606**(3), 508–537 (1996). https://doi.org/10.1016/0375-9474(96)00187-X
29. S. Kubis, M. Kutschera, Nuclear matter in relativistic mean field theory with isovector scalar meson. Phys. Lett. B **399**(3), 191–195 (1997). https://doi.org/10.1016/S0370-2693(97)00306-7
30. B. Liu, V. Greco, V. Baran, M. Colonna, M. Di Toro, Asymmetric nuclear matter: the role of the isovector scalar channel. Phys. Rev. C **65**, 045201 (2002). https://doi.org/10.1103/PhysRevC.65.045201
31. B. Kumar, S.K. Patra, B.K. Agrawal, New relativistic effective interaction for finite nuclei, infinite nuclear matter, and neutron stars. Phys. Rev. C **97**, 045806 (2018). https://doi.org/10.1103/PhysRevC.97.045806
32. V. Thakur, R. Kumar, P. Kumar et al., Effects of an isovector scalar meson on the equation of state of dense matter within a relativistic mean field model. Phys. Rev. C **106**, 045806 (2022). https://doi.org/10.1103/PhysRevC.106.045806
33. S. Wang, H.F. Zhang, J.M. Dong, Neutron star properties in density-dependent relativistic mean field theory with consideration of an isovector scalar meson. Phys. Rev. C **90**, 055801 (2014). https://doi.org/10.1103/PhysRevC.90.055801
34. T.F. Motta, A.M. Kalaitzis, S. Antić, P.A.M. Guichon, J.R. Stone, A.W. Thomas, Isovector effects in neutron stars, radii, and the GW170817 constraint. Astrophys. J. **878**(2), 159 (2019). https://doi.org/10.3847/1538-4357/ab218e
35. F. Li, B.-J. Cai, Y. Zhou, W.-Z. Jiang, L.-W. Chen, Effects of isoscalar- and isovector–scalar meson mixing on neutron star structure. Astrophys. J. **929**(2), 183 (2022). https://doi.org/10.3847/1538-4357/ac5e2a
36. S. Kubis, W. Wójcik, D.A. Castillo, N. Zabari, Relativistic mean-field model for the ultracompact low-mass neutron star HESS J1731-347. Phys. Rev. C **108**, 045803 (2023). https://doi.org/10.1103/PhysRevC.108.045803
37. S. Weissenborn, D. Chatterjee, J. Schaffner-Bielich, Hyperons and massive neutron stars: the role of hyperon potentials. Nucl. Phys. A **881**, 62–77 (2012). https://doi.org/10.1016/j.nuclphysa.2012.02.012
38. D. Chatterjee, I. Vidaña, Do hyperons exist in the interior of neutron stars? Eur. Phys. J. A **52**(2), 29 (2016). https://doi.org/10.1140/epja/i2016-16029-x
39. E. Farhi, R.L. Jaffe, Strange matter. Phys. Rev. D **30**, 2379–2390 (1984). https://doi.org/10.1103/PhysRevD.30.2379
40. P. Haensel, J.L. Zdunik, R. Schaefer, Strange quark stars. Astron. Astrophys. **160**(1), 121–128 (1986)
41. M. Alford, D. Blaschke, A. Drago et al., Quark matter in compact stars? Nature **445**(7125), E7–E8 (2007). https://doi.org/10.1038/nature05582
42. M.G. Alford, S. Han, K. Schwenzer, Signatures for quark matter from multi-messenger observations. J. Phys. G Nucl. Part. Phys. **46**(11), 114001 (2019). https://doi.org/10.1088/1361-6471/ab337a
43. O. Ivanytskyi, D. Blaschke, Density functional approach to quark matter with confinement and color superconductivity. Phys. Rev. D **105**, 114042 (2022). https://doi.org/10.1103/PhysRevD.105.114042
44. E. Annala, T. Gorda, J. Hirvonen, O. Komoltsev, A. Kurkela, J. Nättilä, A. Vuorinen, Strongly interacting matter exhibits deconfined behavior in massive neutron stars. Nat. Commun. **14**(1), 8451 (2023). https://doi.org/10.1038/s41467-023-44051-y
45. J. Bramante, N. Raj, Dark matter in compact stars. Phys. Rep. **1052**, 1–48 (2024). https://doi.org/10.1016/j.physrep.2023.12.001
46. F. Ma, W. Guo, C. Wu, Kaon meson condensate in neutron star matter including hyperons. Phys. Rev. C **105**, 015807 (2022)
47. V.B. Thapa, M. Sinha, Dense matter equation of state of a massive neutron star with antikaon condensation. Phys. Rev. D **102**, 123007 (2020). https://doi.org/10.1103/PhysRevD.102.123007
48. C.-H. Lee, Kaon condensation in dense stellar matter. Phys. Rep. **275**(5), 255–341 (1996). https://doi.org/10.1016/0370-1573(96)00005-1
49. N.K. Glendenning, J. Schaffner-Bielich, Kaon condensation and dynamical nucleons in neutron stars. Phys. Rev. Lett. **81**, 4564–4567 (1998). https://doi.org/10.1103/PhysRevLett.81.4564
50. G.E. Brown, C.-H. Lee, M. Rho, Recent developments on kaon condensation and its astrophysical implications. Phys. Rep. **462**(1), 1–20 (2008). https://doi.org/10.1016/j.physrep.2008.03.002
51. J.A. Pons, S. Reddy, P.J. Ellis, M. Prakash, J.M. Lattimer, Kaon condensation in proto-neutron star matter. Phys. Rev. C **62**, 035803 (2000). https://doi.org/10.1103/PhysRevC.62.035803
52. T. Malik, S. Banik, D. Bandyopadhyay, Equation-of-state table with hyperon and antikaon for supernova and neutron star merger. Astrophys. J. **910**(2), 96 (2021). https://doi.org/10.3847/1538-4357/abe860
53. L. Baiotti, Gravitational waves from neutron star mergers and their relation to the nuclear equation of state. Prog. Part. Nucl. Phys. **109**, 103714 (2019). https://doi.org/10.1016/j.ppnp.2019.103714
54. B.P. Abbott, R. Abbott, T.D. Abbott et al., GW170817: measurements of neutron star radii and equation of state. Phys. Rev. Lett. **121**, 161101 (2018). https://doi.org/10.1103/PhysRevLett.121.161101
55. E. Annala, T. Gorda, A. Kurkela, A. Vuorinen, Gravitational-wave constraints on the neutron-star-matter equation of state. Phys. Rev.

Lett. **120**, 172703 (2018). https://doi.org/10.1103/PhysRevLett.120.172703
56. C.A. Raithel, F. Özel, D. Psaltis, Tidal deformability from GW170817 as a direct probe of the neutron star radius. Astrophys. J. **857**(2), L23 (2018). https://doi.org/10.3847/2041-8213/aabcbf
57. R. Nandi, P. Char, S. Pal, Constraining the relativistic mean-field model equations of state with gravitational wave observations. Phys. Rev. C **99**, 052802 (2019). https://doi.org/10.1103/PhysRevC.99.052802
58. A. Kanakis-Pegios, P.S. Koliogiannis, C.C. Moustakidis, Speed of sound constraints from tidal deformability of neutron stars. Phys. Rev. C **102**, 055801 (2020). https://doi.org/10.1103/PhysRevC.102.055801
59. A. Kedia, H.I. Kim, I.-S. Suh, G.J. Mathews, Binary neutron star mergers as a probe of quark-hadron crossover equations of state. Phys. Rev. D **106**, 103027 (2022). https://doi.org/10.1103/PhysRevD.106.103027
60. H.C. Das, A. Kumar, S.K. Patra, Effects of dark matter on the inspiral properties of the binary neutron stars. Mon. Not. R. Astron. Soc. **507**(3), 4053–4060 (2021). https://doi.org/10.1093/mnras/stab2387
61. B. Hong, Z. Ren, Mixed dark matter models for the peculiar compact object in remnant HESS J1731-347 and their implications for gravitational wave properties. Phys. Rev. D **109**, 023002 (2024). https://doi.org/10.1103/PhysRevD.109.023002
62. N. Zabari, S. Kubis, W. Wójcik, Influence of the interactions of scalar mesons on the behavior of the symmetry energy. Phys. Rev. C **99**, 035209 (2019). https://doi.org/10.1103/PhysRevC.99.035209
63. B.G. Todd-Rutel, J. Piekarewicz, Neutron-rich nuclei and neutron stars: a new accurately calibrated interaction for the study of neutron-rich matter. Phys. Rev. Lett. **95**, 122501 (2005). https://doi.org/10.1103/PhysRevLett.95.122501
64. G.A. Lalazissis, J. König, P. Ring, New parametrization for the Lagrangian density of relativistic mean field theory. Phys. Rev. C **55**, 540–543 (1997). https://doi.org/10.1103/PhysRevC.55.540
65. F.J. Fattoyev, C.J. Horowitz, J. Piekarewicz, B. Reed, GW190814: impact of a 2.6 solar mass neutron star on the nucleonic equations of state. Phys. Rev. C **102**, 065805 (2020). https://doi.org/10.1103/PhysRevC.102.065805
66. W.-C. Chen, J. Piekarewicz, Searching for isovector signatures in the neutron-rich oxygen and calcium isotopes. Phys. Lett. B **748**, 284–288 (2015). https://doi.org/10.1016/j.physletb.2015.07.020
67. V. Thakur, R. Kumar, P. Kumar, V. Kumar, B.K. Agrawal, S.K. Dhiman, Relativistic mean field model parametrizations in the light of GW170817, GW190814, and PSR J0740 + 6620. Phys. Rev. C **106**, 025803 (2022). https://doi.org/10.1103/PhysRevC.106.025803
68. T. Miyatsu, M.-K. Cheoun, K. Kim, K. Saito, Can the PREX-2 and CREX results be understood by relativistic mean-field models with the astrophysical constraints? Phys. Lett. B **843**, 138013 (2023). https://doi.org/10.1016/j.physletb.2023.138013
69. N. Hornick, L. Tolos, A. Zacchi, J.-E. Christian, J. Schaffner-Bielich, Relativistic parameterizations of neutron matter and implications for neutron stars. Phys. Rev. C **98**, 065804 (2018). https://doi.org/10.1103/PhysRevC.98.065804
70. W.-C. Chen, J. Piekarewicz, Building relativistic mean field models for finite nuclei and neutron stars. Phys. Rev. C **90**, 044305 (2014). https://doi.org/10.1103/PhysRevC.90.044305
71. C.J. Horowitz, J. Piekarewicz, B. Reed, Insights into nuclear saturation density from parity-violating electron scattering. Phys. Rev. C **102**, 044321 (2020). https://doi.org/10.1103/PhysRevC.102.044321
72. E. Khan, J. Margueron, I. Vidaña, Constraining the nuclear equation of state at subsaturation densities. Phys. Rev. Lett. **109**, 092501 (2012). https://doi.org/10.1103/PhysRevLett.109.092501
73. P.-G. Reinhard, X. Roca-Maza, W. Nazarewicz, Information content of the parity-violating asymmetry in ^{208}Pb. Phys. Rev. Lett. **127**, 232501 (2021). https://doi.org/10.1103/PhysRevLett.127.232501
74. N.K. Glendenning, J. Schaffner-Bielich, First order kaon condensate. Phys. Rev. C **60**, 025803 (1999). https://doi.org/10.1103/PhysRevC.60.025803
75. T. Maruyama, H. Fujii, T. Muto, T. Tatsumi, Kaon condensation and equation of state in the relativistic mean-field theory. Phys. Lett. B **337**, 19–24 (1994). https://doi.org/10.1016/0370-2693(94)91436-2
76. P.J. Ellis, R. Knorren, M. Prakash, Kaon condensation in neutron star matter with hyperons. Phys. Lett. B **349**, 11–17 (1995). https://doi.org/10.1016/0370-2693(95)00231-9
77. G.H. Wang, W.J. Fu, Y.X. Liu, Remarks concerning kaon condensation in neutron stars. Phys. Rev. C **76**, 065802 (2007). https://doi.org/10.1103/PhysRevC.76.065802
78. G.Y. Shao, Y.X. Liu, Influence of the isovector–scalar channel interaction on neutron star matter with hyperons and antikaon condensation. Phys. Rev. C **82**, 055801 (2010). https://doi.org/10.1103/PhysRevC.82.055801
79. S. Banik, D. Bandyopadhyay, Third family of superdense stars in the presence of antikaon condensates. Phys. Rev. C **64**, 055805 (2001). https://doi.org/10.1103/PhysRevC.64.055805
80. V. Koch, K^--proton scattering and the λ (1405) in dense matter. Phys. Lett. B **337**, 7–13 (1994). https://doi.org/10.1016/0370-2693(94)91434-6
81. M. Lutz, Nuclear kaon dynamics. Phys. Lett. B **426**, 12–20 (1998). https://doi.org/10.1016/S0370-2693(98)00299-8
82. E. Friedman, A. Gal, J. Mareš, A. Cieplý, K^--nucleus relativistic mean field potentials consistent with kaonic atoms. Phys. Rev. C **60**, 024314 (1999). https://doi.org/10.1103/PhysRevC.60.024314
83. A. Bhattacharyya, I.N. Mishustin, W. Greiner, Deconfinement phase transition in compact stars: Maxwell versus Gibbs construction of the mixed phase. J. Phys. G Nucl. Part. Phys. **37**(2), 025201 (2010). https://doi.org/10.1088/0954-3899/37/2/025201
84. C. Constantinou, T. Zhao, S. Han, M. Prakash, Framework for phase transitions between the Maxwell and Gibbs constructions. Phys. Rev. D **107**, 074013 (2023). https://doi.org/10.1103/PhysRevD.107.074013
85. E. Burns, Neutron star mergers and how to study them. Living Rev. Relativ. **23**(1), 4 (2020). https://doi.org/10.1007/s41114-020-00028-7
86. C. Huang, G. Raaijmakers, A.L. Watts et al., Constraining a relativistic mean field model using neutron star mass–radius measurements I: nucleonic models. Mon. Not. R. Astron. Soc. **529**(4), 4650–4665 (2024). https://doi.org/10.1093/mnras/stae844
87. G. Raaijmakers, S.K. Greif, K. Hebeler et al., Constraints on the dense matter equation of state and neutron star properties from NICER's mass–radius estimate of PSR J0740+6620 and multi-messenger observations. Astrophys. J. Lett. **918**(2), L29 (2021). https://doi.org/10.3847/2041-8213/ac089a
88. N. Rutherford, G. Raaijmakers, C. Prescod-Weinstein, A. Watts, Constraining bosonic asymmetric dark matter with neutron star mass-radius measurements. Phys. Rev. D **107**, 103051 (2023). https://doi.org/10.1103/PhysRevD.107.103051
89. M. Ferreira, C. Providência, Constraining neutron star matter from the slope of the mass–radius curves. Phys. Rev. D **110**, 063018 (2024). https://doi.org/10.1103/PhysRevD.110.063018
90. G. Pratten, P. Schmidt, N. Williams, Impact of dynamical tides on the reconstruction of the neutron star equation of state. Phys. Rev. Lett. **129**, 081102 (2022). https://doi.org/10.1103/PhysRevLett.129.081102

91. E.R. Most, L.R. Weih, L. Rezzolla, J. Schaffner-Bielich, New constraints on radii and tidal deformabilities of neutron stars from GW170817. Phys. Rev. Lett. **120**, 261103 (2018). https://doi.org/10.1103/PhysRevLett.120.261103
92. C.-N. Luo, S.-P. Tang, J.-L. Jiang, W.-H. Gao, D.-M. Wei, The bulk properties of isolated neutron stars inferred from the gravitational redshift measurements. Astrophys. J. **930**(1), 4 (2022). https://doi.org/10.3847/1538-4357/ac6175
93. S. Chatterjee, K.K. Nath, Insights into neutron stars from gravitational redshifts and universal relations. arXiv:2502.04943 (2025)
94. J.A. Faber, F.A. Rasio, Binary neutron star mergers. Living Rev. Relativ. **15**(1), 8 (2012). https://doi.org/10.12942/lrr-2012-8
95. D. Radice, S. Bernuzzi, A. Perego, The dynamics of binary neutron star mergers and GW170817. Annu. Rev. Nucl. Part. Sci. **70**(1), 95–119 (2020). https://doi.org/10.1146/annurev-nucl-013120-114541
96. L. Blanchet, Gravitational radiation from post-Newtonian sources and inspiralling compact binaries. Living Rev. Relativ. **9**(1), 4 (2006). https://doi.org/10.12942/lrr-2006-4
97. M. Boyle, D.A. Brown, L.E. Kidder, A.H. Mroué, H.P. Pfeiffer, M.A. Scheel, G.B. Cook, S.A. Teukolsky, High-accuracy comparison of numerical relativity simulations with post-Newtonian expansions. Phys. Rev. D **76**, 124038 (2007). https://doi.org/10.1103/PhysRevD.76.124038
98. A. Buonanno, B. S. Sathyaprakash, Sources of gravitational waves: theory and observations (2015). https://doi.org/10.48550/arXiv.1410.7832. arXiv:1410.7832
99. L. Blanchet, G. Faye, F. Larrouturou, The quadrupole moment of compact binaries to the fourth post-Newtonian order: from source to canonical moment. Class. Quantum Gravity **39**(19), 195003 (2022). https://doi.org/10.1088/1361-6382/ac840c
100. A. Chattaraj, T. RoyChowdhury, Divyajyoti, C.K. Mishra, A. Gupta, High accuracy post-Newtonian and numerical relativity comparisons involving higher modes for eccentric binary black holes and a dominant mode eccentric inspiral-merger-ringdown model, Phys. Rev. D **106**, 124008 (2022). https://doi.org/10.1103/PhysRevD.106.124008
101. B.D. Lackey, The neutron-star equation of state and gravitational waves from compact binaries, Ph.D. thesis, The University of Wisconsin-Milwaukee (2012)
102. M. Maggiore, *Gravitational Waves: Volume 1: Theory and Experiments* (Oxford University Press, Oxford, 2007). https://doi.org/10.1093/acprof:oso/9780198570745.001.0001
103. A. Buonanno, B.R. Iyer, E. Ochsner, Y. Pan, B.S. Sathyaprakash, Comparison of post-Newtonian templates for compact binary inspiral signals in gravitational-wave detectors. Phys. Rev. D **80**, 084043 (2009). https://doi.org/10.1103/PhysRevD.80.084043
104. K. Hotokezaka, K. Kyutoku, M. Shibata, Exploring tidal effects of coalescing binary neutron stars in numerical relativity. Phys. Rev. D **87**, 044001 (2013). https://doi.org/10.1103/PhysRevD.87.044001
105. K. Hotokezaka, K. Kyutoku, Y. Sekiguchi, M. Shibata, Measurability of the tidal deformability by gravitational waves from coalescing binary neutron stars. Phys. Rev. D **93**, 064082 (2016). https://doi.org/10.1103/PhysRevD.93.064082
106. L.E. Kidder, Using full information when computing modes of post-Newtonian waveforms from inspiralling compact binaries in circular orbit. Phys. Rev. D **77**, 044016 (2008). https://doi.org/10.1103/PhysRevD.77.044016
107. Q. Henry, Complete gravitational-waveform amplitude modes for quasicircular compact binaries to the 3.5PN order. Phys. Rev. D **107**, 044057 (2023). https://doi.org/10.1103/PhysRevD.107.044057
108. G. Faye, S. Marsat, L. Blanchet, B.R. Iyer, The third and a half-post-Newtonian gravitational wave quadrupole mode for quasi-circular inspiralling compact binaries. Class. Quantum Gravity **29**(17), 175004 (2012). https://doi.org/10.1088/0264-9381/29/17/175004
109. S.E. Perkins, N. Yunes, E. Berti, Probing fundamental physics with gravitational waves: the next generation. Phys. Rev. D **103**, 044024 (2021). https://doi.org/10.1103/PhysRevD.103.044024
110. M. Punturo, M. Abernathy, F. Acernese et al., The third generation of gravitational wave observatories and their science reach. Class. Quantum Gravity **27**(8), 084007 (2010). https://doi.org/10.1088/0264-9381/27/8/084007
111. S. Dwyer, D. Sigg, S.W. Ballmer, L. Barsotti, N. Mavalvala, M. Evans, Gravitational wave detector with cosmological reach. Phys. Rev. D **91**, 082001 (2015). https://doi.org/10.1103/PhysRevD.91.082001
112. M. Evans, R.X. Adhikari, C. Afle et al., A horizon study for cosmic explorer: science, observatories, and community. arXiv:2109.09882 (2021). https://doi.org/10.48550/arXiv.2109.09882
113. M. Bailes, B.K. Berger, P.R. Brady et al., Gravitational-wave physics and astronomy in the 2020s and 2030s. Nat. Rev. Phys. **3**, 344–366 (2021). https://doi.org/10.1038/s42254-021-00303-8
114. P. Jaranowski, A. Królak, Gravitational-wave data analysis. Formalism and sample applications: the gaussian case. Living Rev. Relativ. **8**, 3 (2005). https://doi.org/10.12942/lrr-2005-3
115. M. Vallisneri, Use and abuse of the fisher information matrix in the assessment of gravitational-wave parameter-estimation prospects. Phys. Rev. D **77**, 042001 (2008). https://doi.org/10.1103/PhysRevD.77.042001
116. C. Cutler, E.E. Flanagan, Gravitational waves from merging compact binaries: how accurately can one extract the binary's parameters from the inspiral waveform? Phys. Rev. D **49**, 2658–2697 (1994). https://doi.org/10.1103/PhysRevD.49.2658
117. L.S. Finn, D.F. Chernoff, Observing binary inspiral in gravitational radiation: one interferometer. Phys. Rev. D **47**, 2198–2219 (1993). https://doi.org/10.1103/PhysRevD.47.2198
118. B.P. Abbott, R. Abbott, T.D. Abbott, S. Abraham et al., Prospects for observing and localizing gravitational-wave transients with Advanced LIGO, Advanced Virgo and KAGRA. Living Rev. Relativ. **23**(1), 3 (2020). https://doi.org/10.1007/s41114-020-00026-9
119. L. Blanchet, B.R. Iyer, B. Joguet, Gravitational waves from inspiraling compact binaries: energy flux to third post-newtonian order. Phys. Rev. D **65**, 064005 (2002). https://doi.org/10.1103/PhysRevD.65.064005
120. J. Vines, E.E. Flanagan, T. Hinderer, Post-1-Newtonian tidal effects in the gravitational waveform from binary inspirals. Phys. Rev. D **83**, 084051 (2011). https://doi.org/10.1103/PhysRevD.83.084051